

Vol. 3 • No. 7 • July 2022

ADVANCED PHOTONICS RESEARCH

Open Access

WILEY-VCH

www.advphotonicsres.com

Two-Photon Nanomachining of a Micromechanically Enhanced Optical Cavity Sensor on an Optical Fiber Tip

Jeremiah C. Williams, Hengky Chandralalim,* Joseph S. Suelzer, and Nicholas G. Usechak

Herein, a two-photon nanostructuring process that is employed to monolithically integrate dynamic three-dimensional (3D) micromechanical features into Fabry–Pérot cavity (FPC) sensors on an optical fiber tip is demonstrated. These features represent a breakthrough in the integration and fabrication capabilities of micro optomechanical devices and systems. The demonstrated dynamic optical surface enables directional thin-film deposition onto obscured areas. The rotation of the dynamically movable mirror to deposit a thin reflective coating onto the inner surfaces of a FPC with curved geometry is leveraged. The reflective coating in conjunction with the dynamically rotatable mirror greatly improves the quality factor of the FPC and enables a new class of highly integrated multi-purpose sensor systems. A unique open cavity geometry on an optical fiber tip is used to demonstrate temperature and refractive index sensing with sensitivities of 2045 ± 39 nm/RIU and 366 ± 22 pm °C⁻¹, respectively. A gold reflective coating sputtered onto the inner surfaces of the FPC improves the quality factors of the cavity by more than 800%. This technology presents a path forward for utilizing 3D design freedom in micromechanically enhanced optical systems to facilitate versatile processing and advantageous geometries beyond the current state of the art.

miniaturized sensors are essential for applications such as satellites,^[1] wearables,^[2] and unmanned aerial systems,^[3] which have stringent size, weight, and power (SWAP) requirements. Reducing the footprint of these sensors while retaining performance frees valuable system resources. Fiber optics integrated with micro FP resonators represent a promising approach to miniaturize a variety of sensors that are essential in modern engineering systems. Fiber optics offer light weight, low losses over long distances, and immunity to electromagnetic interference while serving as an integrated waveguide to introduce and interrogate light. The FP resonator delivers a highly sensitive optical response to a variety of environmental stimuli. Notably, microscale FP cavities exhibit both high sensitivities and large operating ranges at common commercial wavelengths and demonstrate high-quality factors (*Q*-factors) with standard reflective coatings.

1. Introduction

The primary purpose of the dynamically adjustable optical cavity in this work is to enable reflective coating deposition onto the obscure optical surfaces of a multipurpose fiber tip cavity sensor to improve the optical response of the device. High-quality

Fiber optics with integrated FP resonators are represented in the literature with a variety of designs and applications. Devices have been demonstrated sensing static pressure,^[4–21] temperature,^[4,7,9,10,12–16,20,22–37] refractive index (RI) of liquid and gas,^[5,22,23,38–40] magnetic field strength,^[41] airflow,^[42–44] liquid flow vector,^[45] humidity,^[46,47] acoustic pressure,^[48,49] ultrasound,^[50] vibration,^[51] and applied force.^[52] All these exciting applications could be improved by utilizing reflective coatings and curved surfaces, as enabled by the dynamically movable hinged mirror feature demonstrated in this work. Our technology can also be used to isolate a resonator's temperature dependence to create multifunctional sensors.

Several creative manufacturing techniques have been explored to achieve microscale optical cavities. For example, both closed and open cavities have been demonstrated by splicing single-mode fiber (SMF) to short segments of capillary or internally structured fiber.^[8,10,22,23,42] Open cavities have also been made by removing fiber material with a focused ion beam (FIB)^[30] or femtosecond laser.^[39] Curved surfaces have been fashioned with polymer droplets^[7,13] and the electrical arc of a fiber splicer.^[22,38] Various materials with advantageous properties have been integrated with devices to improve performance including polyvinyl chloride (PVC),^[19] silicone rubber,^[18] silicon,^[21,29,45] liquid mercury,^[28] Nafion,^[46] silver film,^[17]

J. C. Williams, H. Chandralalim
Department of Electrical and Computer Engineering
The Air Force Institute of Technology
Wright–Patterson Air Force Base, OH 45433, USA
E-mail: hengky@microsystems.group

J. S. Suelzer, N. G. Usechak
Sensors Directorate
Air Force Research Laboratory
Wright–Patterson Air Force Base, OH 45433, USA

 The ORCID identification number(s) for the author(s) of this article can be found under <https://doi.org/10.1002/adpr.202100359>.

© 2022 The Authors. Advanced Photonics Research published by Wiley-VCH GmbH. This is an open access article under the terms of the Creative Commons Attribution License, which permits use, distribution and reproduction in any medium, provided the original work is properly cited.

DOI: 10.1002/adpr.202100359

polyvinyl alcohol (PVA),^[47] high temperature ceramics,^[6] and selectively sintered stainless steel.^[26] Thin silica films have also been demonstrated by precise etching with hydrofluoric acid (HF)^[16] or etching with HF and fusing to an external silica membrane.^[15] Reflective coatings have been integrated directly in various stages of fabrication^[6,14,17] and through microelectromechanical systems (MEMS) adhered to the fiber.^[8,9,11,49]

While impressive, most fabrication techniques are limited to simple geometries such as planar surfaces or large bubbles. Reflective coatings must also be carefully planned throughout the fabrication process as internal optical surfaces are often obscured in the final device. Additive manufacturing techniques enable arbitrary 3D features, such as curved mirrors. Two popular methods for additive manufacturing on optical fibers are stereolithography and two-photon polymerization (2PP) nanofabrication. Stereolithography has been used to fabricate an open FP resonator^[5] and a closed FP resonator with an integrated antireflective microstructure.^[4] 2PP nanofabrication offers even greater precision and has been used to demonstrate complicated 3D features on optical fiber tips with submicron accuracy. Examples include a force-sensitive microgripper,^[53] multilens objectives,^[54] micro-ring resonators,^[55] whispering gallery mode resonators,^[56,57] an inverse-designed metalens,^[58] a micro-anemometer,^[43,44] a microphone,^[59] and FP cavity sensors.^[12,20,24,27,37,40,41,47,48,52,60,61] This work utilizes 2PP nanofabrication to demonstrate a design solution that enables directional thin-film deposition onto a monolithically integrated optical cavity with dynamic mirrors of arbitrary curvature.

Dual purpose sensors have been demonstrated by combining a fiber Bragg grating (FBG) sensor with an FP resonator^[46] and by utilizing two in-line FP resonators.^[7,10,13,14,16,22,23] With two FP resonators, one cavity can be designed to shift only in response to temperature, while the second cavity responds to both temperature and another physical property, such as pressure or environmental RI. Thus, the temperature response (inherent to all FP resonators due to thermomechanical and thermo-optic effects) of the dual-purpose sensor can be isolated from its other sensing function. Our research group desires to create such a dual-cavity, self-referencing device with three curved optical surfaces, reflective coatings, and advanced micro-mechanical features by utilizing 2PP nanofabrication.

A mechanically suspended two-cavity device with curved surfaces was demonstrated in our previous works,^[24] but the inner optical surface was shadowed by the top surface that prevented reflective coating deposition. Depositing a gold reflective film by sputtering improved the *Q*-factor of the FP resonator as shown in Figure S1b, Supporting Information. However, the measured spectrum (blue curve in Figure S1b, Supporting Information) was consistent with resonance between the topmost and bottom-most optical surfaces only, eliminating the optical response of the inner cavity. This work presents dynamic 3D optomechanical features that address the aforementioned issues.

The micromechanically enabled optical cavity was fabricated using the highly selective, submicron accuracy of 2PP nanofabrication method. The design in combination with two-photon nanostructuring process facilitates precise, directional thin film deposition onto all available optical surfaces in the proposed FP resonator. The implemented mechanical hinge successfully enabled deposition onto the previously obscured surface, creating

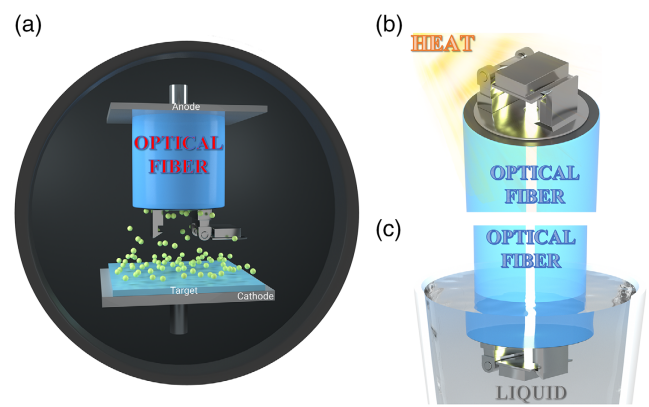


Figure 1. a) A schematic highlighting the monolithically integrated movable mirror that enables directional deposition of highly reflective coating onto the inner surfaces of an FPC using a ubiquitously available magnetron sputtering system. Schematic illustrations of b) a thermal radiation sensor and c) a refractive index sensor on an optical fiber tip.

an optical resonator between the two inner surfaces. These devices also demonstrated thermal radiation and RI sensing, showcasing the feasibility of a multipurpose sensor utilizing this technology. **Figure 1a** highlights the movable mirror that enables directional deposition of highly reflective thin film onto the inner surfaces of an FPC using a widely available magnetron sputtering system. After the thin reflective coating is sputtered onto the inner surfaces of the cavity, the rotatable mirror is locked into its final position. A unique open cavity geometry on an optical fiber tip can be used to monitor the quality of the surrounding environment and how it changes over time as illustrated in Figure 1b,c. The detected changes can then be transmitted in real-time via low-loss optical fibers to different remote locations.

2. Results and Discussion

2.1. A Mechanically Enhanced Fabry–Pérot Resonator

The FP resonator is a ubiquitous optical component formed by two parallel, partially reflective surfaces separated by some interstitial medium. Light is introduced propagating perpendicular to the cavity, along the optical axis of the resonator. By tuning the wavelength of the incident light or changing the cavity length, the transmitted light cycles between constructive and destructive interference. The wavelength or cavity is resonant when the constructive interference is the largest. A graphical depiction of this interaction in our devices is displayed in **Figure 2**.

The FP resonator has been well modeled in other literature, with a thorough example found in^[62] and relevant relationships repeated here. The time necessary for light to traverse the resonator cavity and return to its entry point (the round-trip time t_{RT}) is determined by the length of the cavity L and RI of the interstitial medium within the cavity n , and given by $t_{RT} = \frac{2Ln}{c}$, where c is the speed of light in vacuum. This round trip introduces a phase shift ϕ_{RT} to light of wavelength λ equal to, $\phi_{RT} = 2\pi \frac{c}{\lambda} t_{RT} = \frac{4\pi Ln}{\lambda}$. Resonance repeats after a phase shift equal to a multiple m of 2π , yielding the resonant wavelength λ_m to be, $2\pi m = \frac{4\pi Ln}{\lambda_m} \rightarrow \lambda_m = \frac{2Ln}{m}$. Differentiating this equation for λ_m with

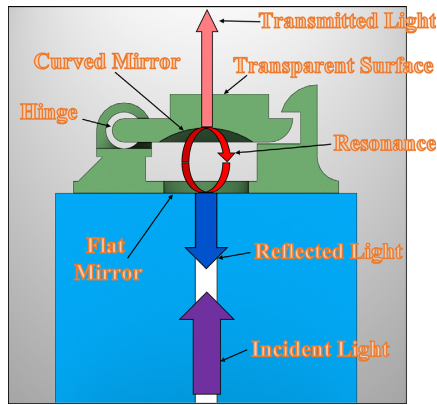


Figure 2. A cross-sectional schematic illustrating the operation of the mechanically enhanced 3D FP resonator and optical fiber as an integrated waveguide for the device.

respect to L and n for a single mode order and taking a linear approximation^[63] yields

$$\frac{\Delta\lambda_m}{\lambda_m} = \frac{\Delta n}{n_0} + \frac{\Delta L}{L_0} \quad (1)$$

where L_0 , n_0 , and λ_m are the initial values of cavity's length, RI, and resonant wavelength, respectively. Equation (1) summarizes the sensing mechanism of our devices. Small changes in cavity length and RI produce small changes in the resonant wavelength. One can measure this optical response to observe any environmental phenomena that affects L or n over a large range with high sensitivity.

The ideal response of a FP resonator is modeled with an Airy function, which can be analyzed as the sum of individual resonant modes represented with Lorentzian profiles.^[62] Normalized to a maximum transmission value of one, the ideal Lorentzian shape of a FP resonator's transmission intensity, I_t , at a single resonant mode in terms of the incident light's wavelength is given by

$$I_t(\lambda) = \frac{1}{\pi} \frac{\left(\frac{\Delta\lambda_{FWHM}}{\lambda_2\lambda_1}\right)^2}{\left(\frac{\Delta\lambda_{FWHM}}{\lambda_2\lambda_1}\right)^2 + 4(\lambda^{-1} - \lambda_m^{-1})^2}, \quad I_t(\lambda_m) = 1 \quad (2)$$

where $\Delta\lambda_{FWHM}$ is the full width at half maximum (FWHM) of the resonance feature and λ_2 and λ_1 are the endpoints in this bandwidth. Equation (2) represents transmission through the cavity, while our work utilizes reflection from the cavity. Ideally, all light incident to the cavity is either reflected or transmitted such that $I_T = I_r + I_t$ where I_T is the total incident intensity, I_r is the reflected intensity, and I_t is the transmitted intensity. The FWHM is determined by the reflectivity of the optical surfaces of the cavity. For two surfaces of reflectance R , the FWHM is related to R by $-\ln(R^2)/2 = 2\pi L n \Delta\lambda_{FWHM} / \lambda_2 \lambda_1$.^[62] Higher reflectivity yields finer resonant features, which drive superior sensitivity, sensing range, and signal clarity. A common metric used to evaluate resonant features is the quality factor Q , given by $Q = \lambda_m / \Delta\lambda_{FWHM}$.

The open cavity device was designed to interrogate its surrounding environment. The dynamically rotatable hinged mirror

enables directional deposition of a reflective coating material onto the inner surface of a FPC, which reduces the FWHM and raises the optical Q -factor of the cavity.

The hinge comprises a pin, housing, support material, and latch. The hinge pin has a diameter of $10 \mu\text{m}$ and a clearance of $2.5 \mu\text{m}$ between the housing. Five $1\text{-}\mu\text{m}$ pillars connect the pin to the housing during polymerization. The latch serves to both hold and align the hinged mirror in its final position. Curvature on the lip of the mirror and top of the latch allow the latch to flex when being pressed into place.

The hinged mirror is curved to reduce walk-off losses as light resonates within the cavity and to improve misalignment sensitivity. The mirror has a nominal radius of curvature of $35 \mu\text{m}$. When closed, the curved mirror is $22\text{--}27 \mu\text{m}$ above the flat mirror of the fiber face, placing the focal point beyond the surface of the fiber. This design meets the criteria for a stable hemispherical resonator configuration, a condition that reduces losses as light resonates within the cavity.^[64]

This geometry was found to be the most successful of the different cavities we explored. The shorter cavity length produces a larger free spectral range (FSR) between resonance features but makes it difficult for viscous and cohesive fluids to enter the cavity. For our design, the smaller cavity length also significantly reduced misalignment caused by the clearances around the hinge pin and the latch, permitting sustained resonance at higher reflectance values. **Figure 3** illustrates graphical representations of the optical cavity in several orientations to showcase its micromechanical features.

To sense thermal radiation, the open cavity device experiences thermal deformation ΔL proportional to its coefficient of thermal expansion α given by $\Delta L = L_0 \alpha \Delta T$, where L_0 is the initial cavity length, and ΔT is the change in temperature. The RI within the cavity changes slightly with the air temperature, which can be predicted with the Ciddor technique.^[65] This Δn is a lot smaller compared to the ΔL from thermal deformation. The peak of the resonant feature moves linearly according to Equation (1). Changes in the RI of the cavity's interstitial medium also shifts the resonant wavelength linearly as directly predicted by Equation (1).

2.2. Two-Photon Nanomachining Process

Devices were fabricated using 2PP nanofabrication in a 2PP system, the Nanoscribe Photonic Professional GT. This technique is similar to stereolithography 3D printing, in which a liquid resin is selectively solidified by a laser that imparts the polymerization energy of the resin. This same polymerization energy can be achieved with two photons of light at half the frequency needed for single photon polymerization. The volume within the laser beam capable of performing 2PP is much smaller than the volume capable of performing single photon polymerization. This produces an extremely small voxel (3D pixel) that can be guided through the resin to solidify the desired volume. This work utilized a $200 \text{ nm} \times 200 \text{ nm} \times 200 \text{ nm}$ voxel to fabricate the optical cavity with monolithically integrated swivel mirror.

In short, single mode optical fiber was first cleaved using a Fujikura CT-30 high-precision fiber cleaver. It was then mounted into a Newport FPH-S fiber chuck, with a small portion

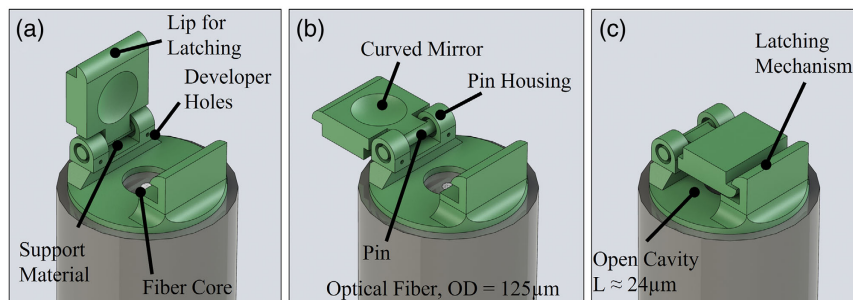


Figure 3. Graphics depicting the three positions of the optical cavity. a) The device immediately after fabrication, before manipulating the mirror with a semiconductor analysis probe. b) The device in the fully open position, when the reflective film is deposited by a magnetron sputtering system. c) The device in the closed position, when it can be readily used for sensing.

(≈ 0.5 mm) extended out the end of the chuck. A drop of UV-curable resin, Nanoscribe's IP-DIP, was then deposited onto the end of the fiber chuck, enveloping the fiber tip. The chuck was affixed to a custom 3D printed jig, which was mounted to a sample holding plate. The top light of the laser inscription system was removed to allow clearance for this mounting assembly.

The 63x objective of the laser inscription system was then raised to contact the resin droplet. The cleaved face of the fiber was located manually by the operator. Light was coupled to the fiber with a UV-safe light-emitting diode (LED) flashlight. The lit core was used to align the structure to the fiber face. A 5 μm thick pad was included as the base of the optical cavity to ensure adhesion to the fiber face. The starting height of the adhesion pad was selected manually by the operator to be below the surface of the fiber. This ensured polymerization began as close to the surface of the fiber as possible and secured the polymerized structure to the fiber. This technique introduced a variability of 5 μm to the final cavity length, which can be reduced by automating

fabrication. For all theoretical calculations in this work, ideal cavity length of 24 μm was used.

Each device was designed using Solidworks 3D computer-aided design (CAD) software. The solid model was divided into thin layers by Nanoscribe's slicer software. Each layer was solidified by a mode-locked 780 nm laser with a 120 fs pulse duration, 80 MHz repetition rate, and 10 mm s^{-1} scan speed directed by galvanometric control. The laser inscription process flow is highlighted in **Figure 4** and animated in Video S1, Supporting Information. The nonpolymerized resin was developed away in propylene glycol methyl ether acetate (PGMEA) for 20 min. After 10 min, the fiber was extended several millimeters to avoid resin collecting on the fiber tip. The device was then cleaned in isopropyl alcohol (IPA) for 10 min. Total fabrication time, including fiber preparation/mounting, polymerization, and chemical treatments, was about 50 min.

Although 2PP nanofabrication is considerably faster than other nanofabrication techniques, the stepwise laser writing

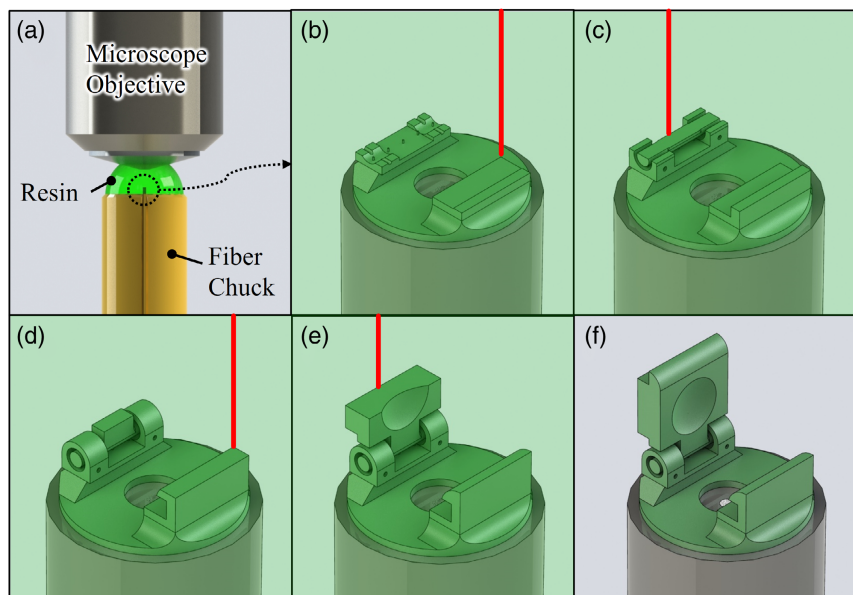


Figure 4. A graphical highlight of the 2PP fabrication process with the rotatable top mirror cavity device. a) The microscope objective is immersed in a drop of resin on top of the fiber chuck surrounding the fiber tip. b–e) Various stages of the two-photon polymerization process, as the device is constructed according to the sliced CAD file. f) The final optical cavity with a freely rotatable top mirror after the unexposed resin is washed away.

process presented striations into the surface finish of the fabricated structures. Hemispherical FP cavities require an optically smooth spherical mirror, and it was uncertain if the devices created here had an optical-quality surface finish. Also of concern, features with a height equal to one half or one quarter of the wavelength of interest could introduce destructive interference and create an antireflective surface. To analyze the surface finish, we fabricated a sample structure onto a glass slide to mount into an atomic force microscope (AFM). The resultant AFM scan is reported in Figure S2, Supporting Information. The surface roughness from the stepwise laser writing process was present at regular intervals. The surface finish was found to have a roughness of less than 75 nm. This work focused on using wavelengths in the 1450–1650 nm range to probe the FP structures fabricated on the fiber ends. Therefore, the surface roughness is significantly smaller than the wavelengths of interest, and far less than one half or one quarter wavelength interval which would lead to their own interference effects.

An initial study was performed to identify suitable highly reflective coating materials that can be deposited on the inner optical surfaces of the cavity to improve its reflectivity. Glass slides (76 mm × 24 mm × 1 mm) were coated on each side with thin film dielectrics and metals. Series of measurements to select a coating material that yields the highest optical Q -factor were performed according to the experimental setup in Figure S3a, Supporting Information. Results plotted in Figure S3b, Supporting Information, suggest that 20 nm of gold deposited by a magnetron sputtering system should be employed as a reflective coating material to enhance the Q -factor of the cavity.

In order to deposit a thin film of gold, the top rotatable mirror was moved into the fully open position with a semiconductor

analysis probe as demonstrated in Video S2, Supporting Information. Manually manipulating the top rotatable mirror required dexterity similar to precise wire-bonding or device probing. A thin layer of gold was then deposited onto the interior of the hinged mirror and the fiber face by a magnetron sputtering system. The sputtering parameters for the device are listed in Table S1, Supporting Information. The hinged mirror was manipulated to the fully open position, such that the inner curved surface was parallel to the fiber face and facing away from the fiber surface (Figure 1a). Both the curved surface and fiber face were oriented toward the sputtering target by holding the fiber in a custom spring-loaded jig. The open cavity device was positioned in the center of the chamber on a rotating platen, with the target facing the platen at an acute angle. The hinged mirror was then lowered into its final position, again using a semiconductor analysis probe as demonstrated in Video S3, Supporting Information. The flexibility of the solidified polymer allowed moderately aggressive manipulations without breaking the device. The false-colored scanning electron microscope (SEM) images of the fabricated fiber tip FPC in open and closed positions are shown in Figure 5a,b. The optical microscope images of semiconductor probe tip micro-manipulations at several steps to open and close the top mirror of the cavity are presented in Figure 5c–f.

2.3. Characterization of a Mechanically Enhanced Fiber Tip Fabry–Pérot Resonator

The fabricated cavity was characterized according to the experimental setup described in Figure 6a. The key component to isolate the reflection spectrum out of the cavity was the optical

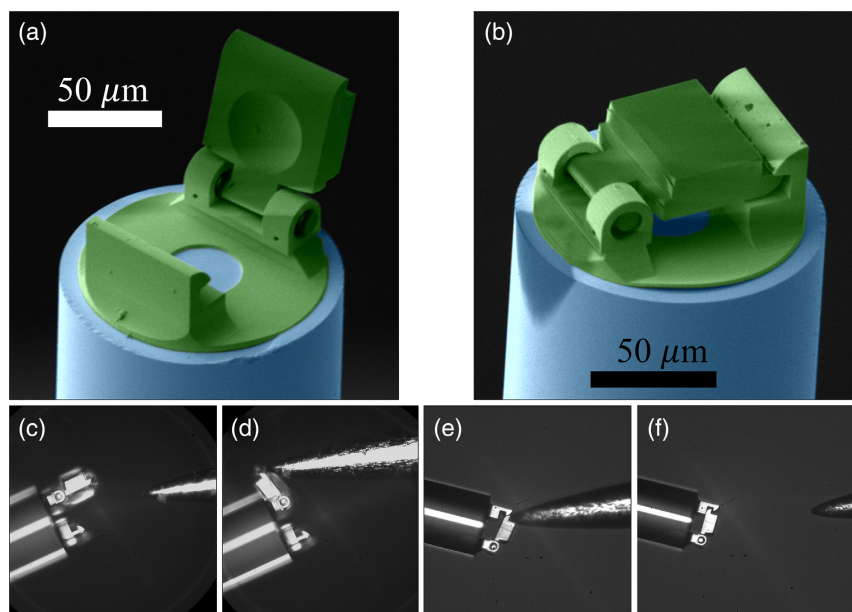


Figure 5. False-colored SEM images of the fabricated fiber tip FPC (green) in various positions on the tip of an optical fiber (blue). a) The FPC in the half-open position when the device was fabricated. b) The FPC in the closed position when the fabrication was completed. Optical microscope images capturing the micro-manipulations used to fabricate the devices. c) The cavity as fabricated on an optical fiber tip with the micromanipulator probe approaching from the right. d) The semiconductor analysis probe was used to open the hinged mirror. Sputtering occurred with the device in this position. e,f) The probe was used to lower the hinged mirror and lock it into its final position.

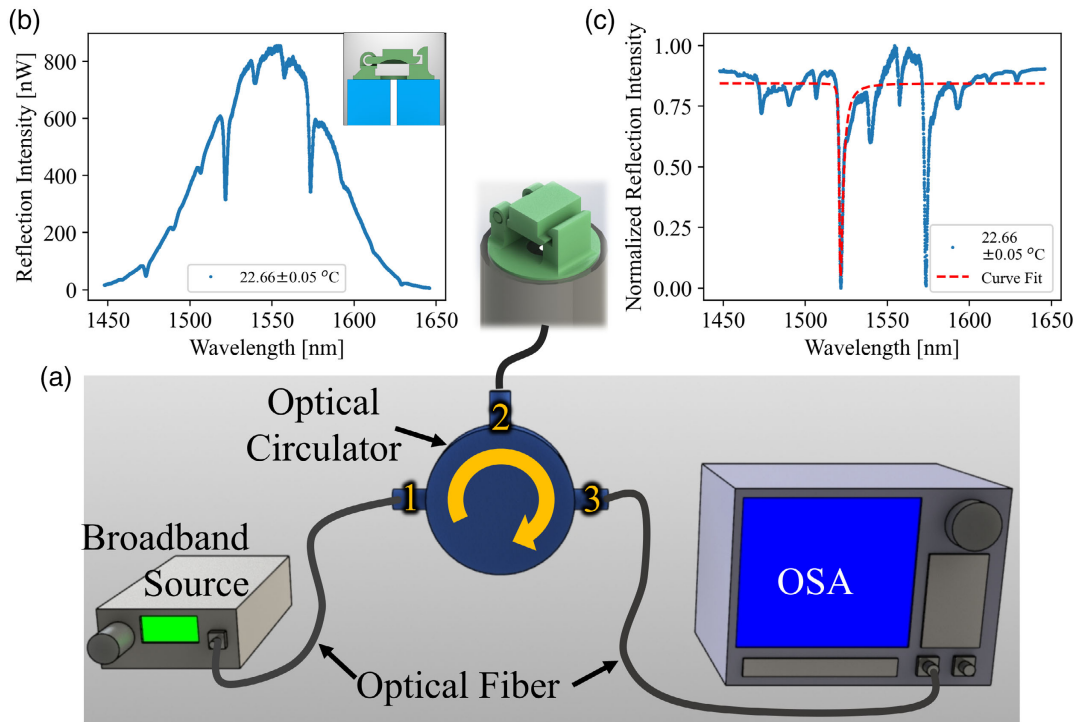


Figure 6. a) A schematic describing the experimental setup used to characterize the reflection intensity of the fabricated FPC on an optical fiber tip. b) The preprocessed reflection spectrum of the FPC in air at room temperature. c) The same reflection spectrum after subtracting the baseline spectral power dependence profile of the SLD and normalizing between minimum and maximum reflection values. The red dashed line shows the result of fitting Equation (3) to a chosen resonance feature.

circulator. This component was a standard fiber-optic device which transmitted light from port one to two and two to three (with ≈ 1 dB of insertion loss) and prevented transmission in the opposite direction (≈ 40 dB of attenuation). A fiber-coupled superluminescent diode (SLD) broadband source (BBS), the Thorlabs S5FC1550SP-A2, was connected to port one, which emitted a 200 nm spectrum centered at 1550 nm. The intensity of the SLD was wavelength dependent, but the profile of this dependence can be easily subtracted from the device measurements. The fabricated device under test was connected to port two. The reflection spectrum from the device was isolated and routed through port three to a Yokogwa AQ6370C optical spectrum analyzer (OSA).

The baseline wavelength power dependence of the BBS was recorded from the average of five measurements of the BBS routed directly into the OSA, removing the effects of the optical circulator. This baseline was subtracted from each measured reflection spectrum of the devices. The magnitude of the response was then normalized to the minimum and maximum reflection intensity of that reading. Measurements plotted before and after this processing are presented in Figure 6b,c. The ideal output of the FP resonator is the airy function, which can be analyzed as the sum of individual resonant features with Lorentzian profiles.^[62] Individual resonant features were analyzed in this work to evaluate the shift produced by the environmental stimuli with higher fidelity than analyzing the entire spectral response. The peak wavelength and FWHM of the resonant features were approximated by fitting a generic skew-Lorentzian distribution to

500 points around each feature. The generic skew-Lorentzian expression^[66] used for the fitting is

$$I_r(\lambda) = 1 - \frac{A}{\pi\theta[1 + (\frac{\lambda-c}{\theta})^2]} \left(1 + \frac{\gamma(\lambda-c)}{\sqrt{\theta^2 + (1 + \gamma^2)(\lambda-c)^2}} \right) + B \quad (3)$$

Best-fit values were found for A , a scaling factor, B , an offset factor, c , the center wavelength of a nonskewed curve, θ , the FWHM of a nonskewed curve, and γ , the skew factor. Both c and θ lost their physical meaning on a skewed curve, so the peak and FWHM were calculated from the output of the fit using the BBS wavelength spectrum from the experiment as the input. The curve was subtracted from one, which represented full transmission, to properly orient the feature as a dip rather than a peak. The curve generated by fitting Equation (3) to the measured reflection data is presented in Figure 6c.

Equation (3) was chosen for the functional model because it can capture the asymmetry observed around the resonant features and more accurately identified the minimum of the spectral response, which was used to indicate changes in the cavity. The asymmetrical response has been observed in prior literature and was attributed to a phase shift introduced by a high reflective metal coating near the limited aperture in a SMF.^[67] This skewed shape was also present in multimode fiber FP resonators and was attributed to multiple resonant modes propagating within the cavity near the ideal resonant wavelength.^[68] The Q -factors

and reflectance values for the mirrors can be extracted from the curve fits using Equation (2) and the expression $Q = \lambda_m / \Delta\lambda_{FWHM}$. A gold reflective coating sputtered onto the inner optical surfaces demonstrated Q -factor and reflectance values of 530 ± 8 and 0.8296 ± 0.0022 .

2.4. Environmental Monitoring using a Mechanically Enhanced Fiber Tip Fabry–Pérot Resonator

The unique open cavity geometry on an optical fiber tip naturally provides an interstitial space that can be utilized to perform various environmental monitoring tasks. The detected information can be directly transmitted through low-loss optical fibers to different remote locations. The FPC sensors can work with a ubiquitously available white light source, thereby facilitating the realization of highly compact, economical, and versatile sensors. Here, we demonstrate the capability of a FPC sensor in detecting changes in temperature and RI.

2.4.1. Refractive Index Sensing

The fiber tip FPC sensor was immersed in a mixture of IPA and water according to the experimental setup in Figure 7a to measure changes in RI of the liquid. The IPA concentration in the solution was varied from 40% to 100% by volume to achieve RI

values from 1.3610 to 1.3773. Solutions less than 40% IPA were unable to enter the cavity, due to the stronger cohesion of water and the small opening at the side of the cavity. The solutions were prepared by measuring the prescribed volumes of IPA and water with a micro-pipette, depositing them into a glass vial, and stirring vigorously. Samples of this mixture were measured in a commercial refractometer, the Mettler Toledo 30GS, to verify the RI of the solution. Five samples of each mixture were measured for reference. This refractometer utilized a wavelength of 589.3 nm for measurement. The device fiber was mounted into a side loading fiber chuck and immersed into the vial with the remaining liquid sample. The device was left in the solution for approximately 15 min, with agitation introduced as needed to remove any bubbles that formed around the fiber. Holding the device in the solution for this time reduced drift that was observed in early readings. The reflection spectrum was then measured five times. Three reflection spectra from the device in different solutions are plotted in Figure 7b.

The resonant wavelength of the device shifted linearly in response to the RI of liquid within the cavity. This response is presented in Figure 7c. The blue points represent the mean value of the central resonant wavelength from the five measurements. Vertical error bars represent one standard deviation of this measurement, and horizontal error bars represent one standard deviation of the RI measured by the Mettler Toledo refractometer. The dashed red line shows the linear fit to the data.

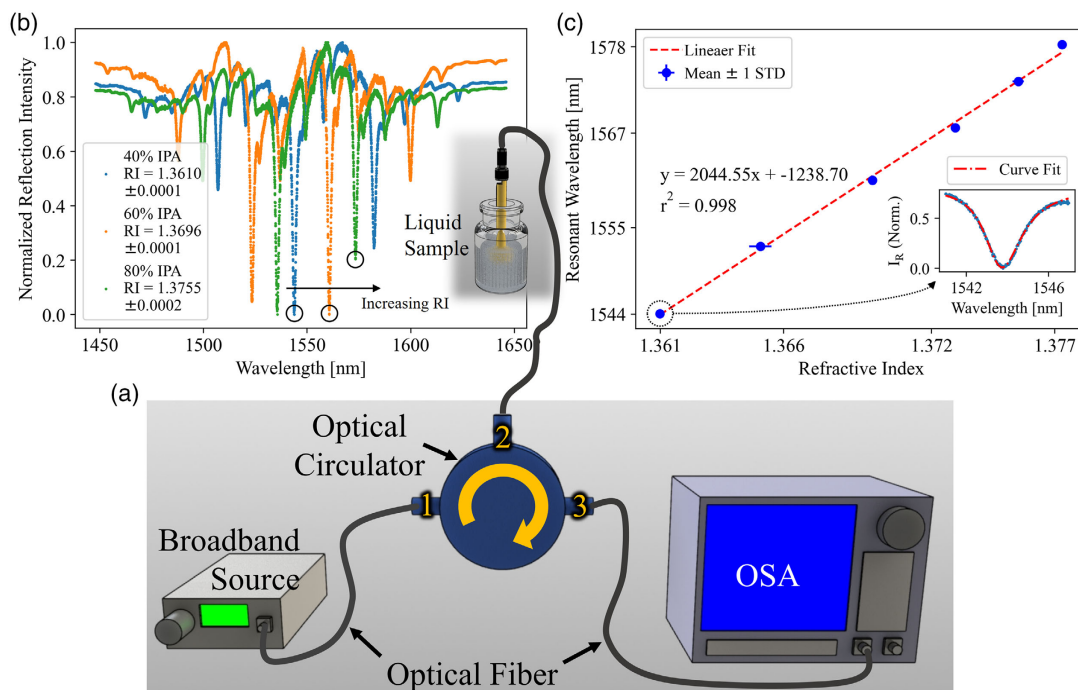


Figure 7. a) A schematic describing the experimental setup used to characterize the performance of a FPC RI sensor on an optical fiber tip. b) Three reflection spectra from the device in different solutions. Each response has been normalized between its minimum and maximum reflection values and had the SLD's baseline spectral power dependence profile subtracted. The primary resonant features are noted with an arrow showing increasing RI, while smaller, off-axis resonant features can be seen between the primary features. c) The locations of peak wavelengths of the primary resonant features as extracted from fitting a skewed Lorentzian distribution to the reflection spectrum at the RI values measured on the Mettler Toledo reference refractometer. The points represent the mean of five measurements taken at a given RI, the vertical error bars represent one standard deviation of these measurements, and the horizontal error bars represent one standard deviation of the mean of the RI measured by the reference refractometer. The red, long dashed line represents the linear fit to this data. The inset shows an example of the fitted curve on top of the reflection intensity measured from the 40% IPA sample.

The linear fit reveals a sensitivity of approximately 2045 ± 39 nm per refractive index unit (RIU). The uncertainty listed represents the 95% confidence interval of the slope in the linear fit. The locking mechanism to secure the top mirror provides sufficient mechanical stability as indicated by the error bars in Figure 7c.

Using the skewed-Lorentzian fit, we calculated an average Q -factor of 703 ± 12 , and a mirror reflectance of 0.8287 ± 0.0029 . Simulations indicated that misalignment as small as 0.3° can reduce the Q -factor of a resonant feature by nearly half.^[68] Thus, significant improvement should result by further refining our technology to better align the rotatable mirror to the fiber face. Future devices could utilize an adhesive or an additional micromechanical feature such as a cam or shim to secure the hinged mirror and maintain proper alignment, thus increasing Q -factors. Additionally, on-chip FP cavity resonators have demonstrated Q -factors as high as 10^5 by utilizing dielectric stacks for reflective surfaces,^[69] which could be easily implemented with the mechanically adjustable optics.

Secondary resonant dips with lower intensity were present accompanying the primary features and can be seen between the primary dips in Figure 7b. These secondary resonant dips were caused by off-axis resonant modes enabled by the curved mirror.^[63] These features were linked to the same inner cavity and not the outer polymer cavity because they shifted in response to RI changes along with the primary feature. The bandwidth between recurring resonant dips and the FSR indicated that this resonance was between the curved mirror and the fiber face, and

not the topmost flat surface. The relationship between FSR and cavity length, L , was approximated by $\Delta\lambda_{\text{FSR}} \approx \frac{\lambda^2}{2nL}$ for normal incident light.^[62]

2.4.2. Temperature Sensing

The fiber tip FPC sensor was suspended several centimeters above a hotplate that has a temperature controller to measure changes in air temperature above the hotplate as shown in Figure 8a. A thermocouple was suspended at the same height for reference. The hotplate's temperature was varied from 22.66 to 176.67 °C, producing air temperatures from 22.66 to 51.08 °C. Once a temperature was reached, the setup was left to stabilize for approximately five minutes. The reflection spectrum was then measured five times. Three reflection spectra from the device at different temperatures are plotted in Figure 8b.

The resonant wavelength shifted in response to changes in the environmental temperature. A sensitivity of approximately 366 ± 22 pm °C⁻¹ was achieved. The uncertainty listed represents the 95% confidence interval of the slope in the linear fit. The results of this test are reported in Figure 8c. The blue points represent the means of the five measurements at each temperature. The vertical error bars show one standard deviation of these measurements, and the horizontal error bars show one standard deviation of the corresponding reference thermocouple

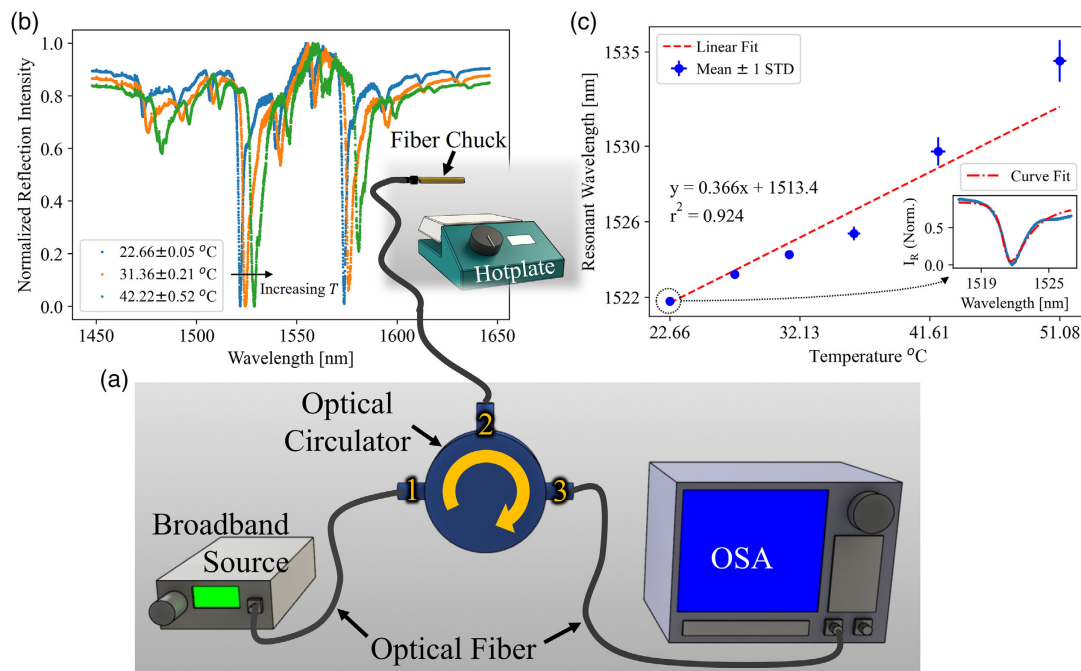


Figure 8. a) A schematic describing the experimental setup used to characterize the performance of an FPC temperature sensor on an optical fiber tip. b) Three reflection spectra from the device at different temperatures. Each response has been normalized between its minimum and maximum reflection values and had the SLD's baseline spectral power dependence profile subtracted. The primary resonant features are noted with an arrow showing increasing temperature, while smaller, off-axis resonant features can be seen between the primary features. c) The locations of peak wavelengths of the primary resonant features as extracted from fitting a skewed Lorentzian distribution at their respective temperatures. The points represent the mean of five measurements taken at a given temperature, the vertical error bars represent one standard deviation of these measurements, and the horizontal error bars represent one standard deviation of the mean of the temperature read on the reference thermocouple. The red, long dashed line represents the linear fit to this data. The inset shows the result of the curve fitting on top of the reflection spectrum measured at 22.66 ± 0.05 °C.

measurements. The dashed line shows the linear fit used to extract the temperature sensitivity of the resonator. Using the equation for thermal expansion, $\Delta L = \alpha L_0 \Delta T$, and the RI shift due to temperature calculated by the Ciddor method,^[65] Equation (1) predicted a wavelength shift of 210 pm/RIU. This value is within the same order of magnitude as our observed results.

Although the mechanically enhanced FPC has the capability of detecting temperature changes, the contact quality between structures made of IP-DIP resin and their substrate is known to degrade at temperatures higher than 450 °C.^[70,71] In addition, the quality of the optical resonance of our device degraded when the temperature of the heat source was set higher than 180 °C. This degradation was due to thermal expansion into the clearance between hinged mirror and its two supports. Imperfect contact to these structures would introduce nonaxial expansions and misalignment that caused instability in the resonant wavelength. This can be mitigated by affixing the hinged mirror after reflective coating deposition, which will also increase the Q -factor of the FPC. At room temperature, the fitting results yielded an average quality factor of 530 ± 8 and mirror reflectance of 0.8296 ± 0.0022 , where the uncertainty is one standard deviation.

3. Conclusion

This work demonstrates a breakthrough combination of design and nanostructuring process for micro optomechanical systems: a dynamically rotatable mirror fabricated with submicron accuracy by selective polymerization to enable integration and fabrication techniques beyond the limits of the current technology. We monolithically integrated this feature to form a FP optical cavity sensor on the tip of an optical fiber to achieve directional deposition of reflective coating onto internal optical surfaces of arbitrary curvature. This capability facilitates the creation of improved, low SWAP, high Q -factors, and micro optomechanical systems for precise multipurpose sensing. Microscale fiber tip sensors with advanced micromechanical features and an enhanced internal cavity were designed and fabricated. They demonstrated sensing of RI and temperature. Sensitivities of 2045 ± 39 nm/RIU for RI sensing and 366 ± 22 pm °C⁻¹ for temperature sensing were achieved. A gold reflective coating sputtered onto the inner surfaces of the optical resonator improved the quality factors of the cavity by more than 800%. We are currently exploring novel locking and self-aligning mechanisms to stabilize the integrated components created by two-photon nanomachining technique. In addition, we are also investigating advanced coating options to improve the Q -factors of future devices. The enhancement of Q -factors by one to two orders of magnitudes will open doors to broader sensing and signal processing applications and support other fundamental scientific endeavors. Overall, the dynamically adjustable 3D micro optomechanical systems demonstrated in this work present a powerful enabling technology for meeting a variety of difficult integration and fabrication challenges that are currently limiting the research progress in microscale optics and optomechanics.

Supporting Information

Supporting Information is available from the Wiley Online Library or from the author.

Acknowledgements

The views expressed in this paper are those of the authors and do not reflect the official policy or position of the USA Air Force, Department of Defense, or the US Government. The authors thank Abigail Juhl and Ecklin Crenshaw for training and assistance with the Nanoscribe and Richard Johnston and Adam Fritzsche for assistance in the AFIT Nanofabrication and Characterization Facility. This work was funded by the Air Force Office of Scientific Research (AFOSR), Grant F4FGA08338J001.

Conflict of Interest

The authors declare no conflict of interest.

Data Availability Statement

The data that support the findings of this study are available from the corresponding author upon reasonable request.

Keywords

3D nanofabrication, Fabry-Pérot, micromechanics, nanomachining, optical fiber sensors, two-photon polymerization

Received: November 27, 2021

Revised: February 27, 2022

Published online:

- [1] P. Ortega, G. López-Rodríguez, J. Ricart, M. Domínguez, L. M. Castañer, J. M. Quero, C. L. Tarrida, J. García, M. Reina, A. Gras, M. Angulo, *IEEE Sens. J.* **2010**, *10*, 1623.
- [2] A. Tricoli, N. Nasiri, S. De, *Adv. Funct. Mater.* **2017**, *27*, 1605271.
- [3] K. Anderson, K. J. Gaston, *Front. Ecol. Environ.* **2013**, *11*, 138.
- [4] J. Wu, M. Yao, F. Xiong, A. P. Zhang, H.-Y. Tam, P. K. A. Wai, *J. Lightwave Technol.* **2018**, *36*, 3618.
- [5] M. Yao, X. Ouyang, J. Wu, A. P. Zhang, H.-Y. Tam, P. K. A. Wai, *Sensors* **2018**, *18*, 1825.
- [6] J. Liu, P. Jia, H. Zhang, X. Tian, H. Liang, Y. Hong, T. Liang, W. Liu, J. Xiong, *Appl. Opt.* **2018**, *57*, 4211.
- [7] X. Tan, X. Li, Y. Geng, Z. Yin, L. Wang, W. Wang, Y. Deng, *IEEE Photonics Technol. Lett.* **2015**, *27*, 2035.
- [8] M. Quan, J. Tian, Y. Yao, *Opt. Lett.* **2015**, *40*, 4891.
- [9] W. Ma, Y. Jiang, J. Hu, L. Jiang, T. Zhang, T. Zhang, *Sens. Actuators A: Phys.* **2020**, *302*, 111795.
- [10] X. Yang, S. Wu, H. Cheng, J. Ma, S. Wang, S. Liu, P. Lu, *Opt. Laser Technol.* **2021**, *140*, 107007.
- [11] G. C. Hill, R. Melamud, F. E. Declercq, A. A. Davenport, I. H. Chan, P. G. Hartwell, B. L. Pruitt, *Sens. Actuators A: Phys.* **2007**, *138*, 52.
- [12] H. Wei, H. Wei, M. Chen, S. Krishnaswamy, *Appl. Opt.* **2020**, *59*, 2173.
- [13] J. M. Coote, E. J. Alles, S. Noimark, C. A. Mosse, C. D. Little, C. D. Loder, A. L. David, R. D. Rakhit, M. C. Finlay, A. E. Desjardins, *Opt. Express* **2019**, *27*, 5641.
- [14] H. Bae, D. Yun, H. Liu, D. A. Olson, M. Yu, *J. Lightwave Technol.* **2014**, *32*, 1585.

- [15] X. Guo, J. Zhou, C. Du, X. Wang, *IEEE Photonics Technol. Lett.* **2019**, 31, 689.
- [16] S. Pevec, D. Donlagic, *Appl. Opt.* **2012**, 51, 4536.
- [17] F. Guo, T. Fink, M. Han, L. Koester, J. Turner, J. Huang, *Opt. Lett.* **2012**, 37, 1505.
- [18] X. Cheng, J. N. Dash, D. S. Gunawardena, L. Htein, H.-Y. Tam, *Sensors* **2020**, 20, 4927.
- [19] Z. Zhang, C. Liao, J. Tang, Z. Bai, K. Guo, M. Hou, J. He, Y. Wang, S. Liu, F. Zhang, Y. Wang, *J. Lightwave Technol.* **2017**, 35, 4067.
- [20] R. K. Poduval, J. M. Coote, C. A. Mosse, M. C. Finlay, A. E. Desjardins, I. Papakonstantinou, *IEEE J. Sel. Top. Quantum Electron.* **2021**, 27, 1.
- [21] Y. Liu, Z. Jing, Z. Jing, R. Li, R. Li, Y. Zhang, Q. Liu, A. Li, C. Zhang, W. Peng, *Opt. Express* **2020**, 28, 948.
- [22] W. Zhang, H. Li, L. Zhu, M. Dong, F. Meng, *IEEE Sens. J.* **2021**, 21, 4635.
- [23] X. Li, S. C. Warren-Smith, L. Xie, H. Ebdorff-Heidepriem, L. V. Nguyen, *IEEE Sens. J.* **2020**, 20, 6408.
- [24] J. W. Smith, J. C. Williams, J. S. Suelzer, N. G. Usechak, H. Chandralalim, *J. Micromech. Microeng.* **2020**, 30, 125007.
- [25] J. W. Smith, J. S. Suelzer, N. G. Usechak, V. P. Tondiglia, H. Chandralalim, in *2019 20th Int. Conf. on Solid-State Sensors, Actuators and Microsystems Eurosensors XXXIII (Transducers Eurosensors XXXIII)*, Berlin, Germany, **2019**, pp. 649–652.
- [26] J. Mathew, C. Hauser, P. Stoll, C. Kenel, D. Polyzos, D. Havermann, W. N. MacPherson, D. P. Hand, C. Leinenbach, A. Spierings, K. Koenig-Urban, R. R. J. Maier, *IEEE Sens. J.* **2017**, 17, 4107.
- [27] M. Li, Y. Liu, R. Gao, Y. Li, X. Zhao, S. Qu, *Sens. Actuators B: Chem.* **2016**, 233, 496.
- [28] K. Yang, J. He, Y. Wang, S. Liu, C. Liao, Z. Li, G. Yin, B. Sun, Y. Wang, *IEEE Photonics J.* **2015**, 7, 1.
- [29] G. Liu, M. Han, W. Hou, *Opt. Express* **2015**, 23, 7237.
- [30] J. Kou, J. Feng, L. Ye, F. Xu, Y. Lu, *Opt. Express* **2010**, 18, 14245.
- [31] H. Chandralalim, J. Smith, US10942313B2, **2021**.
- [32] J. W. Smith, J. C. Williams, S. J. Suelzer, N. G. Usechak, H. Chandralalim, in *Conf. on Lasers and Electro-Optics (2020)*, Paper ATu3K.6, Optical Society of America, San Jose, California, USA, **2020**, p. ATu3K.6.
- [33] H. Chandralalim, J. C. Williams, J. W. Smith, J. S. Suelzer, N. G. Usechak, in *2021 IEEE Research and Applications of Photonics in Defense Conf. (RAPID)*, Miramar Beach, Florida, USA, **2021**, pp. 1–2.
- [34] H. Chandralalim, J. Smith, US11156782B2, **2021**.
- [35] J. Williams, H. Chandralalim, US20210271027A1, **2021**.
- [36] J. Williams, H. Chandralalim, US20210294039A1, **2021**.
- [37] J. Williams, J. Smith, J. S. Suelzer, N. G. Usechak, H. Chandralalim, in *2020 IEEE Sensors*, Rotterdam, Netherlands, **2020**, pp. 1–4.
- [38] C. R. Liao, T. Y. Hu, D. N. Wang, *Opt. Express* **2012**, 20, 22813.
- [39] T. Wei, Y. Han, Y. Li, H.-L. Tsai, H. Xiao, *Opt. Express* **2008**, 16, 5764.
- [40] V. Melissinaki, M. Farsari, S. Pissadakis, *IEEE J. Sel. Top. Quantum Electron.* **2015**, 21, 344.
- [41] D. Zhang, H. Wei, H. Hu, S. Krishnaswamy, *APL Photonics* **2020**, 5, 076112.
- [42] Y. Zhao, P. Wang, R. Lv, X. Liu, *J. Lightwave Technol.* **2016**, 34, 5351.
- [43] J. Williams, J. S. Suelzer, N. G. Usechak, H. Chandralalim, in *2020 IEEE Sensors*, Rotterdam, Netherlands, **2020**, pp. 1–4.
- [44] J. Williams, H. Chandralalim, US20210341320A1, **2021**.
- [45] G. Liu, Q. Sheng, W. Hou, M. Han, *Opt. Lett.* **2016**, 41, 4629.
- [46] S. Liu, Y. Ji, J. Yang, W. Sun, H. Li, *Sens. Actuators A: Phys.* **2018**, 269, 313.
- [47] M. Chen, Y. Zhao, H. Wei, C. Zhu, S. Krishnaswamy, *Sens. Actuators B: Chem.* **2021**, 328, 128981.
- [48] M. Li, Y. Liu, X. Zhao, R. Gao, Y. Li, S. Qu, *Sens. Actuators A: Phys.* **2017**, 260, 29.
- [49] O. Kilic, M. Digonnet, G. Kino, O. Solgaard, *Meas. Sci. Technol.* **2007**, 18, 3049.
- [50] J. A. Guggenheim, J. Li, T. J. Allen, R. J. Colchester, S. Noimark, O. Ogunlade, I. P. Parkin, I. Papakonstantinou, A. E. Desjardins, E. Z. Zhang, P. C. Beard, *Nat. Photonics* **2017**, 11, 714.
- [51] S. Wu, L. Wang, X. Chen, B. Zhou, *J. Lightwave Technol.* **2018**, 36, 2216.
- [52] A. J. Thompson, M. Power, G.-Z. Yang, *Opt. Express* **2018**, 26, 14186.
- [53] M. Power, A. J. Thompson, S. Anastasova, G.-Z. Yang, *Small* **2018**, 14, 1703964.
- [54] T. Gissibl, S. Thiele, A. Herkommer, H. Giessen, *Nat. Photonics* **2016**, 10, 554.
- [55] Q. Liu, Q. Liu, Y. Zhan, Y. Zhan, S. Zhang, S. Feng, X. Wang, W. Sun, J. Ye, Y. Zhang, *Opt. Express* **2020**, 28, 11730.
- [56] S. Zhang, S.-J. Tang, S. Feng, Y.-F. Xiao, W. Cui, X. Wang, W. Sun, J. Ye, P. Han, X. Zhang, Y. Zhang, *Adv. Opt. Mater.* **2019**, 7, 1900602.
- [57] K. Markiewicz, P. Wasylczyk, *Opt. Express* **2019**, 27, 8440.
- [58] W. Hadibrata, H. Wei, S. Krishnaswamy, K. Aydin, *Nano Lett.* **2021**, 21, 2422.
- [59] H. Wang, Z. Xie, M. Zhang, H. Cui, J. He, S. Feng, X. Wang, W. Sun, J. Ye, P. Han, Y. Zhang, *Opt. Laser Technol.* **2016**, 78, 110.
- [60] J. C. Williams, J. S. Suelzer, N. G. Usechak, H. Chandralalim, in *2021 IEEE 34th Int. Conf. on Micro Electro Mechanical Systems (MEMS)*, Gainesville, Florida, USA, **2021**, pp. 382–385.
- [61] J. Williams, H. Chandralalim, US20210325270A1, **2021**.
- [62] N. Ismail, C. C. Kores, D. Geskus, M. Pollnau, *Opt. Express* **2016**, 24, 16366.
- [63] M. H. Bitarafan, R. G. DeCorby, *Sensors* **2017**, 17, 1748.
- [64] A. Yariv, *Quantum Electronics*, Wiley, New York, **1989**.
- [65] P. E. Ciddor, *Appl. Opt.* **1996**, 35, 1566.
- [66] A. Alzaatreh, *MethodsX* **2019**, 6, 938.
- [67] O. Kilic, M. J. F. Digonnet, G. S. Kino, O. Solgaard, *J. Lightwave Technol.* **2009**, 27, 5648.
- [68] A. K. Shaheen, Y. M. Sabry, D. Khalil, *J. Lightwave Technol.* **2021**, 39, 4424.
- [69] W. Wang, C. Zhou, T. Zhang, J. Chen, S. Liu, X. Fan, *Lab Chip* **2015**, 15, 3862.
- [70] M. I. Sharipova, T. G. Baluyan, K. A. Abrashitova, G. E. Kulagin, A. K. Petrov, A. S. Chizhov, A. S. Chizhov, T. B. Shatalova, D. Chubich, D. A. Kolymagin, A. G. Vitukhnovsky, A. G. Vitukhnovsky, V. O. Bessonov, V. O. Bessonov, A. A. Fedyanin, *Opt. Mater. Express* **2021**, 11, 371.
- [71] Y. Liu, H. Wang, J. Ho, R. C. Ng, R. J. H. Ng, V. H. Hall-Chen, E. H. H. Koay, Z. Dong, H. Liu, C.-W. Qiu, J. R. Greer, J. K. W. Yang, *Nat. Commun.* **2019**, 10, 4340.